ACS NANO

www.acsnano.org

ARTICLE

Gate-Tunable Renormalization of Spin-Correlated Flat-Band States and Bandgap in a 2D Magnetic Insulator

Pin Lyu, Joachim Sødequist, Xiaoyu Sheng, Zhizhan Qiu, Anton Tadich, Qile Li, Mark T. Edmonds, Meng Zhao, Jesús Redondo, Martin Švec, Peng Song, Thomas Olsen,* and Jiong Lu*

Cite This: *ACS Nano* 2023, 17, 15441−15448

Read Online

ACCESS | Metrics & More | Article Recommendations | Supporting Information

ABSTRACT: **Emergent quantum phenomena in two-dimensional van der Waal (vdW) magnets are largely governed by the interplay between exchange and Coulomb interactions. The ability to precisely tune the Coulomb interaction enables the control of spin-correlated flat-band states, band gap, and unconventional magnetism in such strongly correlated materials. Here, we demonstrate a gate-tunable renormalization of spin-correlated flat-band states and bandgap in magnetic chromium tribromide ($CrBr_3$) monolayers grown on graphene. Our gate-dependent scanning tunneling spectroscopy (STS) studies reveal that the interflat-band spacing and bandgap of $CrBr_3$ can be continuously tuned by 120 and 240 meV, respectively, *via* electrostatic injection of carriers into the hybrid $CrBr_3$/graphene system. This can be attributed to the self-screening of $CrBr_3$ arising from the gate-induced carriers injected into $CrBr_3$, which dominates over the weakened remote screening of the graphene substrate due to the decreased carrier density in graphene. Precise tuning of the spin-correlated flat-band states and bandgap in 2D magnets *via* electrostatic modulation of Coulomb interactions not only provides effective strategies for optimizing the spin transport channels but also may exert a crucial influence on the exchange energy and spin-wave gap, which could raise the critical temperature for magnetic order.**

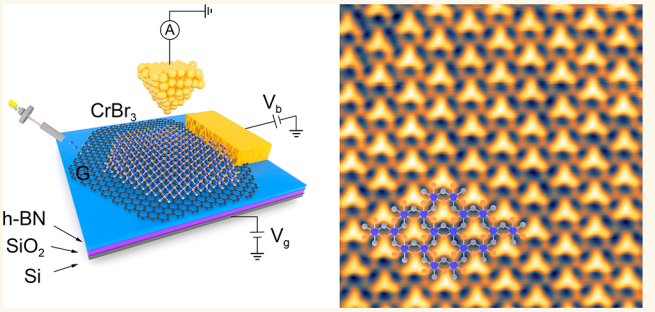

KEYWORDS: *gate-tunable device, 2D magnetic insulator, flat band, band renormalization, STM*

INTRODUCTION

Two-dimensional (2D) van der Waal (vdW) magnets with strong electronic correlations host a variety of exotic quantum phases, including skyrmion,[1] quantum spin liquid,[2] and quantum anomalous hall conductance,[3] and thus these materials have attracted a vast amount of interest following the seminal reports on the layer-dependent magnetism in CrI_3[4] and $CrGeTe_3$[5] crystals. In the 2D limit, the Mermin−Wagner theorem prohibits a spontaneously broken symmetry phase and thus long-range magnetic order arises due to spin−orbit coupling,[6] which explicitly breaks the spin rotational symmetry and leads to magnetic anisotropy. In addition, the interplay between the exchange interaction and strong electronic correlations determines the energy spectrum of the spin-correlated flat-band states as well as the bandgap, which play an essential role in spintronics applications. In particular, the presence of a desired bandgap combined with layer-dependent ferromagnetism enables the integration of 2D magnetic insulators into vdW heterostructures where they may act as tunnel barriers, replacing the traditional dielectrics for next-generation spintronics. Future progress in this field depends on the ability to tune the electronic correlations *via* electrical fields and control the spin-correlated band structures associated with the spin-selective transport barriers in magnetic tunnelling devices.[7,8]

Conventional strategies toward this goal include chemical[9] or electrochemical doping,[10] which are often inflexible and can result in unintentional material degradation. In contrast, electrostatic gating offers a reversible and continuous modulation of the electronic and magnetic properties of the target system, providing excellent compatibility and flexibility

Received: February 3, 2023
Accepted: August 3, 2023
Published: August 8, 2023

for practical electronics and spintronics applications. Despite the recent successes in the experimental realization of electric control of magnetic ordering in 2D magnets,[11−13] electrical modulation of spin-correlated flat-band states and bandgap values has not been demonstrated. Moreover, atomic-scale insights into the influence of gate-controlled carrier densities on electronic correlations remain elusive.

$CrBr_3$ represents an Ising-type ferromagnetic insulator with a Curie temperature of around 34 K[14] and has been proposed to comprise a correlated Mott−Hubbard-like insulator.[15−17] Here, we have taken monolayer $CrBr_3$ as one representative 2D magnetic insulator to probe the gate-tunable renormalization of spin-correlated flat-band states and bandgap using scanning tunneling microscopy (STM). As a direct study of insulating materials *via* STM is infeasible due to lack of a conductive path, one can circumvent this by integrating atomically thin 2D magnetic insulators with conductive layered materials, either by vdW technology[18,19] or molecular beam epitaxy (MBE) growth.[20,21]

To this end, we present an STM/STS study of a magnetic $CrBr_3$ monolayer prepared by MBE on a gate-tunable graphene device. A direct comparison of STS measurements with spin-polarized density functional theory (DFT) calculations enables us to assign each correlated state of $CrBr_3$ to individual spin-split manifolds and to determine the bandgap of monolayer $CrBr_3$ on the graphene substrate. Moreover, we demonstrate a continuous tuning of E_g by 240 meV and the interflat-band spacing between correlated states of $CrBr_3$ by 120 meV through the electrostatic gating. Such experimental observation shows a qualitative agreement with the modulation of on-site Coulomb repulsion energy (U), as revealed in DFT calculation with Hubbard correlations. By directly probing the doping level of the graphene both underneath and near the $CrBr_3$ domain, we find that gate-induced carriers are injected into both $CrBr_3$ (self-screening) and graphene (substrate screening), yielding the opposite effect on the screening. The substrate screening in graphene becomes weaker upon electron doping (reduced hole density), whereas the self-screening in $CrBr_3$ is enhanced.

RESULTS AND DISCUSSION

Structure Characterization of $CrBr_3$ Monolayer on a Back-Gated G/h-BN Device. We carried out MBE growth of monolayer $CrBr_3$ on a back-gated device (Figure 1a), consisting of a chemical vapor deposition (CVD) grown graphene monolayer placed on a 15 nm thick hexagonal boron nitride (h-BN) flake resting on a Si wafer with the 285 nm thick oxide layer (the substrate is denoted as G/h-BN). In contrast to the SiO_2 substrate, the atomic flatness of h-BN dramatically reduces the surface roughness and charge inhomogeneity in graphene, providing an ideal platform for sample growth and subsequent gate-dependent STM measurements. A direct evaporation of anhydrous $CrBr_3$ bulk powder at 400 °C for 30 min allows for the growth of monolayer $CrBr_3$ islands with an apparent height of ∼0.63 nm (inset of Figure 1c) on the back-gated G/h-BN device, as captured in the large-scale STM image (Figure 1c). The closed-up STM image acquired at a sample bias of V_S = 1.2 V reveals the periodic triangular pattern with a characteristic lattice constant of ∼0.64 nm (Figure 1d). The triangular pattern can be correlated to three protruding neighboring Br atoms in the upper layer (marked by orange spheres in atomic model in Figure 1b),

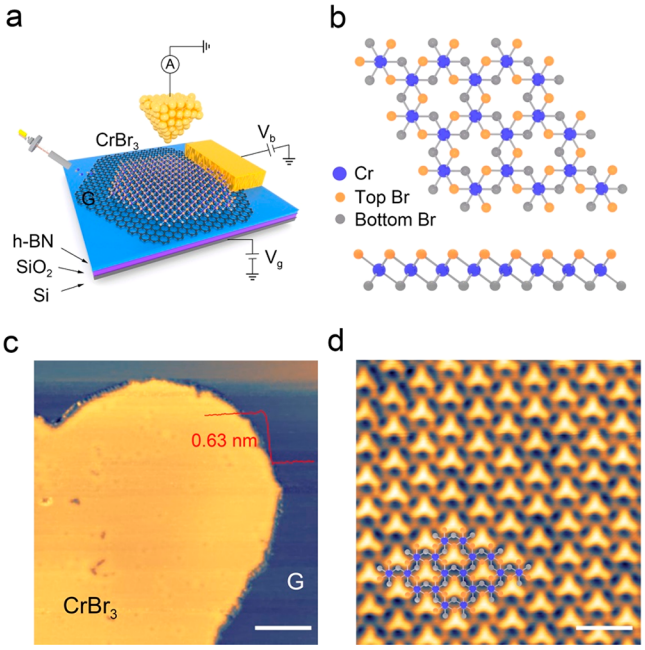

Figure 1. $CrBr_3$ monolayer grown on a back-gated G/h-BN device. (a) Schematic illustration of MBE growth of monolayer $CrBr_3$ islands on a back-gated graphene/h-BN device. (b) Top and side view of the atomic structure of monolayer $CrBr_3$. The top layer of Br atoms is marked as yellow balls, forming a triangular shaped Br trimer. (c) A representative large-scaled STM image of a monolayer $CrBr_3$ island. Inset shows the line profile along the domain edge. Scale bar: 10 nm. Set point: 1.5 V, 10 pA. (d) Atomically resolved STM image of monolayer $CrBr_3$ with the overlaid atomic structure. Scale bar: 1 nm. Set point: 1 V, 10 pA.

consistent with the pattern reported in the previous STM studies of $CrBr_3$.[20−22]

Electronic Properties of $CrBr_3$ Monolayer on the G/h-BN Device. We subsequently performed differential conductance (dI/dV) measurements in order to probe the electronic properties of $CrBr_3$ on this G/h-BN substrate (Figure 2b). The dI/dV spectrum of as-grown monolayer $CrBr_3$ reveals two prominent peaks located at V_S = 1.01 eV (labeled as C_1) and V_S = 1.69 eV (labeled as C_2), and a shallow rise below the Fermi level (E_F) (labeled as V_1). Despite the presence of Moiré structure between graphene and $CrBr_3$, it is not accountable for the experimental observations on renormalization of spin-correlated flat-band states, as reflected in nearly identical spectral features acquired in different Moiré regions (refer to Supporting Information (SI), Figure S1 for more details). To better determine the band edges of $CrBr_3$, we conducted dI/dV measurement at an increased set-point (0.6 V, 100 pA), whereby the intensity of the valence band edge can be dramatically enhanced, turning the shallow rise into a much sharper one (SI, Figure S2). A direct comparison of the dI/dV spectrum taken over monolayer $CrBr_3$ on graphene and on bare graphene enables us to assign a sharp rise at V_S = 0.44 V to the conduction band minimum (CBM) and the kink (onset of the sharp rise) at V_S = 0.85 V to the valence band maximum (VBM), yielding a value for E_g of 1.29 eV for monolayer $CrBr_3$ grown on a G/h-BN substrate (SI, Figure S3, refer to the details of band edge determination in SI, Note 1). It is noted that at a large tip−sample distance (set point: V_S = 1.5V, I_t = 100 pA), the valence band appears featureless as shown in SI, Figure S5, similar to previous

https://doi.org/10.1021/acsnano.3c01038
ACS Nano 2023, 17, 15441−15448

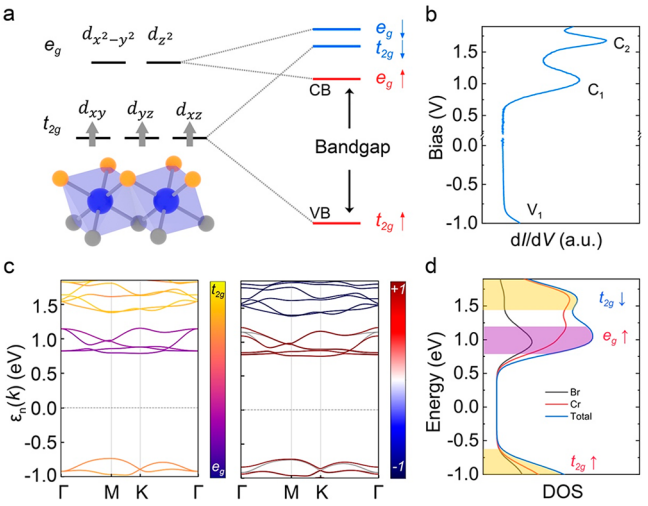

Figure 2. Electronic properties of monolayer $CrBr_3$ on graphene. (a) Schematic illustration of the energy splitting of Cr *d*-orbitals into spin-polarized e_g and t_{2g} bands in the presence of octahedral crystal field and magnetic exchange interactions. (b) Two individual d*I*/d*V* spectra of monolayer $CrBr_3$ at V_g = 0 V are combined. One was taken at a large tip−sample distance (set point: 1.5 V, 100 pA) from 0.2 to 1.8 V, and the other was taken at a reduced tip−sample distance (0.6 V, 100 pA) from −1 to 0.2 V, to better compare and visualize them with the calculated band structure. Two prominent peaks located at V_S = 1.01 eV and V_S = 1.69 eV are labeled as C_1 and C_2, respectively, and the shallow rise below the Fermi level is labeled as V_1. (c) Calculated band structure of monolayer $CrBr_3$ using Perdew−Burke−Ernzerhof (PBE) exchange-correlation functional. The left panel shows the orbital information, where the yellow (purple) color denotes the t_{2g} bands (e_g bands) contributions. The right panel contains the spin information. The red (blue) color denotes the majority-spin (minority-spin) polarization along the out-of-plane direction. Note that SOC was included nonself-consistently in the right panel. (d) Calculated partial DOS of Br *p*-orbitals, Cr *d*-orbitals, and total DOS of a free-standing monolayer $CrBr_3$. Note that the calculated DOS of $CrBr_3$ is manually offset by 0.5 eV to align with the energy position of d*I*/d*V* spectrum.

studies of monolayer $CrBr_3$ grown on graphite[20] and $NbSe_2$[22] substrates. Here, we acquired two individual d*I*/d*V* spectra to probe the valence and conduction bands separately (Figure 2b). One was taken at a large tip−sample distance (set point: V_S = 1.5 V, I_t = 100 pA) from 0.2 to 1.8 V, while the other was taken at a reduced tip−sample distance (set point: V_S = 0.6*V*, I_t = 100 pA) from −1 to 0.2 V. In addition, we observe the E_F is closer to the CBM than the VBM, indicating n-doping of $CrBr_3$, presumably due to charge transfer from the graphene substrate.

To better understand the electronic properties of $CrBr_3$, we performed spin-polarized band structure calculations using the Perdew−Burke−Ernzerhof (PBE) exchange-correlation functional on the Cr atoms (see Methods for details). Each Cr atom is bonded to six Br atoms, which gives rise to an octahedral crystal field that splits the *d*-orbital of Cr atoms into the t_{2g} and e_g manifolds. The spin degeneracy of the these two manifolds is further lifted by magnetic exchange interactions,[23,24] where the energy spacing between the majority and minority spin channels is governed by the effective on-site Coulomb interaction (U)[25] as illustrated in Figure 2a. As shown in Figure 2d, the calculated density of states (DOS) of the free-standing monolayer $CrBr_3$ reproduces the key features observed in the experimental d*I*/d*V* spectrum (Figure 2b). Specifically, the C_1 peak is derived from the spin-majority states ($e_{g,\uparrow}$)) with equal contributions from Cr *d*-orbitals and Br *p*-orbitals, whereas the C_2 peak consists of spin-minority t_{2g} states ($t_{2g,\downarrow}$)) that mainly originate from Cr *d*-orbitals. The calculations reveal that the lowest bands of the unoccupied states are composed of spin-majority states ($e_{g,\uparrow}$) and show a rather flat dispersion with the CBM located at the K point (Figure 2c and SI, Figure S6). In contrast, the VB shows a slightly more dispersive behavior than the CB and the VBM is predicted to be located at the M point. Due to the large in-plane momentum, the electronic states at the M point exhibit a faster out-of-plane decay, which may explain the possible origin for a much weaker d*I*/d*V* signal of the VBM that can only be resolved at a reduced tip−sample distance in the STS measurement.

Gate-Tunable STS Measurements of $CrBr_3$ Monolayer on the G/h-BN Device. Our ability to gate the system allows us to study the fundamental issue of the importance of electron−electron interactions in a strongly correlated system. We do this by measuring how the d*I*/d*V* spectra of $CrBr_3$ evolve as a function of the back-gate voltage (V_g), whereby carrier densities can be tuned continuously (Figure 3b). Gate-dependent STS measurements show that the VBM undergoes a remarkable upward shift in energy from −0.89 ± 0.01 eV to −0.70 ± 0.01 eV, when V_g is increased from −40 to 40 V. In stark contrast, the CBM only shows a slightly downward shift from 0.46 ± 0.01 to 0.41 ± 0.01 eV (SI, Figure S4). The opposite shift between the CBM and VBM leads to a monotonic gap reduction from 1.35 ± 0.01 eV at V_g = -40 V to 1.11 ± 0.01 eV at V_g = 40 V. Furthermore, the C_1 peak shows an upward shift from 0.96 ± 0.01 eV to 1.03 ± 0.01 eV, as V_g is swept from −40 to 40 V, while the C_2 peak moves downward from 1.71 ± 0.01 to 1.66 ± 0.01 eV. This yields a gradual decrease in the interband spacing between C_1 and C_2 from 0.75 ± 0.01 to 0.63 ± 0.01 eV. Parts a and c of Figure 4 show the corresponding energy position of the VBM (cyan), CBM (magenta), C_1 (orange), and C_2 (pink) peaks together with E_g and interband spacing between C_1 and C_2 as a function of V_g. A significant bandgap renormalization of 240 meV is accompanied by a large modulation of the energy separation between the spin-correlated flat-band states (interband spacing between C_1 and C_2), which changes by 120 meV when V_g is varied from −40 to 40 V.

Next, we focus on deciphering the physical origin of the gate-tunable renormalization of the bandgap and spin-correlated flat-band states of monolayer $CrBr_3$. First, we are able to rule out the contribution from the Stark effect due to a negligible field-induced out-of-plane polarization in the 2D monolayer.[26] Second, electrostatic gating may result in charge redistribution, modulating the interfacial dipole, but such an effect can also be excluded because the change in the interfacial dipole causes only a rigid band structure shift and fails to explain the band renormalization observed here (SI, Figure S7). As shown in SI, Figure S8, a set of tip height-dependent STS measurements at different gate voltages can safely rule out the possible origin from the carrier-dependent tip-induced band bending effect (TIBB) to the observed phenomena.[27] We are thus left with gate-tunable carrier density modulation as the key factor governing the renormalization. It has been previously demonstrated that giant bandgap renormalization in 2D materials can be realized by carrier doping, which modulates the Coulomb-hole self-energy and screened-

https://doi.org/10.1021/acsnano.3c01038
ACS Nano 2023, 17, 15441−15448

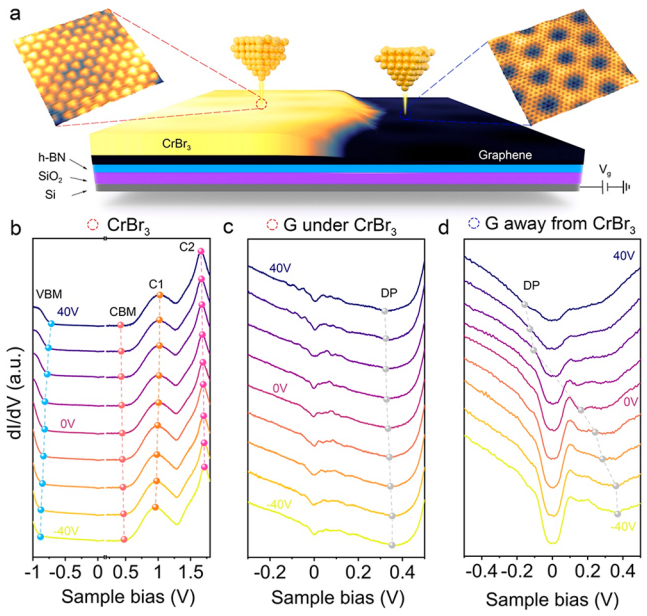

Figure 3. Gate-dependent dI/dV spectra of $CrBr_3$ monolayer on graphene. (a) Schematic illustration of a region containing $CrBr_3$ domain and bare graphene. 3D STM images of $CrBr_3$ domian and bare graphene domain are included. (b) Gate-dependent dI/dV spectra of the monolayer $CrBr_3$ on graphene. The energy position of VBM, CBM, and C_1 and C_2 peaks are indicated by cyan, magenta, orange, and pink points, respectively. Note that at a large tip−sample distance (set point: 1.5 V, 100 pA), the valence band appears featureless. The VBM can be better resolved at a reduced tip−sample distance (0.6 V, 100 pA). dI/dV spectra collected at these two set points are merged to visualize the two band edges simultaneously. (c) Zoom-in dI/dV spectra taken at a closer tip−sample distance over the monolayer $CrBr_3$ on graphene to monitor the Dirac point (DP) position (marked as gray points) as a function of V_g. The Dirac point position is obtained by fitting an inverted Gaussians to the prominent local minimum of each spectrum. Set point: 0.5 V, 200 pA. (d) Gate-dependent dI/dV spectra of a bare graphene surface nearby the monolayer $CrBr_3$ island (10 nm away from the edge of $CrBr_3$ island). The Dirac point is marked as gray points. At V_g = 0 V, graphene/h-BN substrate shows a slightly p-type doping as the E_D of graphene is located at 0.12 eV above the E_F. Set point: 0.5 V, 500 pA.

exchange self-energy.[28,29] Such effects have been experimentally observed in many 2D systems *via* alkali atom deposition.[9,30] Apart from this, increasing the carrier density in the graphene substrate results in effective screening that increases the electron self-energy (quasiparticle stabilization),[31] which typically manifests itself as a quasiparticle bandgap reduction of the adjacent 2D semiconductors in graphene based vdW heterostructures.[32,33] To determine which effect accounts for gate-tunable renormalization, we need to extract the gate-induced carrier density variation in both $CrBr_3$ and the graphene substrate.

One advantage of this study is that we can directly probe the gate-dependent carrier density of the graphene underneath (Figure 3c) and close to the monolayer $CrBr_3$ islands (Figure 3d) *via* dI/dV spectroscopic measurements (refer to SI, Note 3 for the determination of the charge carrier in graphene). The tip−sample distance needs to be further reduced to probe the Dirac point (E_D) of graphene underneath the $CrBr_3$. Here, we used a set point of V_S = 0.5V, I_t = 200 pA to obtain E_D of the underlying graphene. At V_g = 0 V, E_D of the graphene underneath $CrBr_3$ is determined to be 0.32 eV, suggesting a sizable p-doping (n_h = 1.12 × 10^{13} cm^{-2})) of graphene (note that all the E_D values were obtained after subtracting the characteristic phonon energy of graphene[34]). The assignment of E_D of the graphene underneath $CrBr_3$ can be verified by probing the graphene in close proximity to the edge of the $CrBr_3$ island. Upon reaching the edge of the $CrBr_3$ domain, the graphene became heavily p-doped, and the Dirac point position was determined to be E_D = 0.32 eV, consistent with that of graphene beneath $CrBr_3$ (refer to SI, Figures S9−S10 and Note 1 for detailed descriptions of the assignment of E_D). p-doping is due to a significant charge transfer from graphene to $CrBr_3$ arising from the large work function difference between the two materials.[7,35] The charge transfer from graphene to other 2D magnetic materials have been reported by several groups.[36,37] Despite the CBM being positioned away from the Fermi level, the electronic hybridization between graphene and $CrBr_3$ could result in the formation of tail states, which facilitate the injection of charges from graphene into $CrBr_3$.[38] We noted that the E_D of the graphene underneath $CrBr_3$ always lies above E_F, slightly decreasing from 0.34 eV at V_g = −40 to 0.30 eV at V_g = −40 V. This means that the hole carrier density in the graphene substrate undergoes a monotonic decrease from 1.25 × 10^{13} to 1.02 × 10^{13} cm^{-2} within the accessible range of gate voltages. This effect therefore weakens the screening of the Coulomb interactions and is expected to enlarge the bandgap, opposite the trend observed experimentally. In contrast, the E_D of bare graphene close to the $CrBr_3$ domain varies from 0.31 eV at V_g = −40 V (n_h = 5.85 × 10^{12} cm^{-2})) to −0.09 eV at V_g = −40 V (n_e = 0.49 × 10^{12} cm^{-2})), in good agreement with previous study.[34] The gate-induced carrier density variation (Δn = 6.34 × 10^{12} cm^{-2}) on bare graphene is much larger than that on graphene underneath the $CrBr_3$ (Δn = 2.32 × 10^{12} cm^{-2})), suggesting that more carriers are injected into the $CrBr_3$ layer (~4.02 × 10^{12} cm^{-2}) (SI, Figure S11). The gate-induced carriers injected into the $CrBr_3$ layer are expected to enhance the screening of the on-site Coulomb potential, resulting in a bandgap reduction. Therefore, the enhancement of screening resulting from an increase in electron density in $CrBr_3$ by Δn = 4.02 × 10^{12} cm^{-2} dominates over the reduced screening arising from a decrease in hole density by 2.23 × 10^{12} cm^{-2} in graphene. The dominant screening effect from doped carriers in $CrBr_3$ can be rationalized by considering the effective length scale of carrier-induced screening from graphene and $CrBr_3$. Carriers injected into the flat conduction bands of $CrBr_3$ thus generate a more effective self-screening effect on the modulation of effective on-site Coulomb interactions than carriers injected into the graphene substrate.

Because $CrBr_3$ is a strongly correlated material wherein Coulomb interactions play a crucial role in determining its electronic properties, the renormalization of the bandgap and spin-correlated flat-band states caused by gate-induced carriers can be explained as a result of screened on-site Coulomb interactions. To model the local Coulomb interaction between the Cr d electrons, we calculated the DOS of $CrBr_3$ on graphene with different Hubbard corrections (U). It is important to note that the Hubbard corrections applied here can be regarded as effective descriptors that capture the physical effects of screening. The application of Hubbard corrections in DFT is a measure that is typically taken to either correct for delocalization errors or compensate for the fact that the Kohn−Sham gap does not represent the physical gap of a

https://doi.org/10.1021/acsnano.3c01038
ACS Nano 2023, 17, 15441−15448

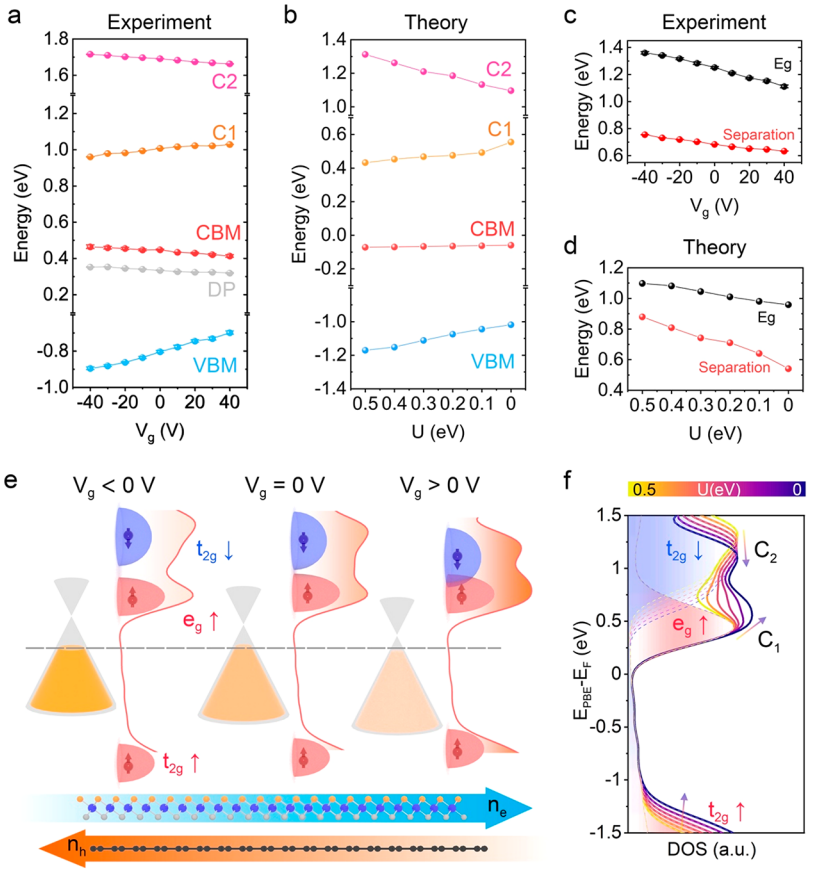

Figure 4. Gate-tunable bandgap renormalization and correlated flat-band states of monolayer $CrBr_3$ on graphene. (a) Energy position of the VBM (cyan), CBM (magenta), Dirac point (gray), C_1 (orange) and C_2 (pink) peaks as a function of gate voltage. (b) Calculated energy position of the VBM (cyan), CBM (magenta), C_1 (orange), and C_2 (pink) peaks as a function of the on-site Coulomb repulsion (U). (c) Measured bandgap and interflat-band spacing between the C_1 and C_2 peaks as a function of gate voltage. (d) Calculated bandgap and interflat-band spacing between the C_1 and C_2 peaks as a function of U. (e) Illustration of the band alignment upon the variation of V_g and the corresponding U. (f) Calculated DOS of monolayer $CrBr_3$ on graphene using different values of U. The C_1 and C_2 peak positions were determined from the numerical maximum of the peak in the projected density of states, and the VBM and CBM was obtained from the slope of the band edges in the projected density of states.

material. It is thus not possible to assign a direct physical meaning to the magnitude of the applied U, but because it represents a screened on-site coulomb interaction, we are able to study the effect of screening by varying the value of U.

If spectral features are represented well at a particular value of U, it is expected that additional screening (gating induced population of the $CrBr_3$ conduction band) should lead to spectral properties that are reproduced by choosing lower values of U. Indeed, our calculations accurately reproduce the spectral features within a range of U values, specifically from 0.5 to 0 eV. In other words, the fact that DFT reproduces the spectral features by lowering the value of U corroborates the interpretation that the physical mechanism for the band shifts is governed by screening. We have only included on-site Coulomb interactions on the Cr d-orbitals, because these are the most localized one (with the largest delocalization error in DFT) and the ones that dominate the spectral features in proximity of the band gap.

Figure 4f shows the calculated DOS of $CrBr_3$ on graphene with different U values separated into two spin channels. We notice that the variation of U governs the spin splitting of the polarized manifolds, where smaller values of U lead to less spin-split manifolds.[25] In addition, a much larger splitting of the t_{2g} manifold than the e_g manifold is likely due to the fact that the t_{2g} manifold has three sets of half-filled orbitals, whereas the e_g manifold has only two sets of empty orbitals. The calculations reveal a monotonic shift of the $t_{2g,\uparrow}$, $t_{2g,\downarrow}$ and $e_{g,\downarrow}$ manifolds upon variation of U, while the $e_{g,\uparrow}$ manifold is pinned at E_F due to the significant charge transfer from graphene to $CrBr_3$. As shown in Figure 4a–d, a direct comparison of the experimental results with the calculated DOS reveals that the bandgap reduction with increased V_g (increased carries density in $CrBr_3$) resembles the band structure evolution with the reduced U. By decreasing U from 0.5 to 0 eV, we observe a bandgap reduction of 140 meV, qualitatively comparable to the experimental value of bandgap reduction achieved by ramping V_g from −40 to +40 V (Δn = 4.02×10^{12} cm $^{-2}$). We thus conclude that the large bandgap renormalization observed here is mainly attributed to the gate-induced electron doping of $CrBr_3$, causing a decrease of U due to the enhanced screening of Coulomb interactions.[39,40]

Apart from the bandgap renormalization, the modulation of U also results in a variation of the spin-correlated flat-band state spacing, namely, the C_1–C_2 separation (the gap between $e_{g,\uparrow}$ and $t_{2g,\downarrow}$ derived flat bands). As illustrated in Figure 2a, both the bandgap and C_1–C_2 separation correlate with the on-site Coulomb energy. Generally, the on-site Coulomb interaction governs the spin-splitting between majority and minority spin

https://doi.org/10.1021/acsnano.3c01038
ACS Nano 2023, 17, 15441−15448

channels, whereas reducing the value of U results in a lower spin splitting. The spin splitting of the t_{2g} bands is significantly larger than that of the e_g band, situating the $t_{2g,\downarrow}$ manifold at higher energies than the $e_{g,\uparrow}$ manifold, and this leads to a modulation of the bandgap defined by the distance between the $e_{g\uparrow}$ and $t_{2g,\uparrow}$ manifolds. The large bare on-site Coulomb repulsion results in a much larger splitting of the t_{2g} bands than the e_g band, which also becomes the dominant effect in determining the bandgap size and interband spacing.

As illustrated in Figure 4e, for a large value of U (U = 0.5 eV, corresponding to V_g < 0 V), the $e_{g,\uparrow}$ and $t_{2g,\downarrow}$ manifolds exhibit a large separation. The $t_{2g,\downarrow}$ manifold contains multiple peak components arising from the splitting of the d_{xy}, d_{yz}, and d_{xz} bands. With decreasing values of U, the $t_{2g,\downarrow}$ manifold moves downward toward EF and its shoulder components start to mix with $e_{g,\uparrow}$ manifold. Hence, for vanishing U (U = 0 eV, corresponding to V_g > 0), orbital mixing between the $e_{g\uparrow}$ and $t_{2g,\downarrow}$ manifold gets enhanced and manifests itself as the emerging C_1 peak, leading to an upward shift of the C_1 peak with respect to the E_F. In addition, the C_2 peak shifts down and results in a significant reduction of interflat-band spacing by 340 meV. This is consistent with the trend of gate-tunable energy separation between C_1 and C_2 peaks observed experimentally.

CONCLUSION

In summary, we have demonstrated a gate-tunable bandgap and interflat-band spacing of $CrBr_3$ monolayer by 240 and 120 meV, respectively, *via* electrostatic gating. This renormalization of the band structure of monolayer $CrBr_3$ can be attributed to a dominant self-screening effect arising from the gate-induced carriers injected into $CrBr_3$ rather than graphene. Our findings not only provide insight into the crucial impact of carrier densities in doped 2D magnets but also offer effective strategies for tuning the flat-band states and bandgap renormalization in strongly correlated systems, different from what is typically observed in conventional 2D materials. Moreover, effective modulation of Coulomb interactions in 2D magnets may also significantly modify the exchange energy and spin-wave gap, which could result in higher critical temperatures for magnetic order.[25,41,42]

METHODS

MBE Growth of $CrBr_3$ on Graphene/h-BN Device. The graphene/h-BN substrate was prepared by transferring monolayer CVD graphene[1] onto exfoliated h-BN flakes that rest on a doped Si wafer coated with a 285 nm SiO_2 layer. The graphene/h-BN substrate was then annealed at 400 °C under Ar/H_2 gas in a tube furnace for 5 h to remove possible polymer residues. Electrodes (Ti, 3 nm; Au, 50 nm) were deposited on graphene using the stencil mask technique. Prior to growth, the graphene/h-BN device was degassed at 300 °C for 2 h in UHV. Monolayer $CrBr_3$ islands were grown by the evaporation of anhydrous $CrBr_3$ bulk powder at 400 °C, while the graphene/h-BN device was held at 150 °C for 30 min.

STM/STS Measurements. The STM/STS measurements were conducted in an LT-STM instrument held at 4.5 K with a base pressure lower than 10^{-10} mbar. The STM tip was calibrated spectroscopically on Au(111) substrate. All of the dI/dV spectra were measured through a standard lock-in technique with a modulated voltage of 5 to 20 mV at a frequency of 812 Hz.

DFT Calculations. The DFT calculations have been carried out using the electronic structure package GPAW,[2] which uses the projector augmented wave method and a planewave basis. The 2D $CrBr_3$ on graphene was simulated using a single unit cell of $CrBr_3$ with the experimentally determined lattice parameter and a $\sqrt{7} \times \sqrt{7}$ unit cell of graphene that were strained by 3.98% to match the lattice parameter. The structure was relaxed under the constraint of a fixed unit cell until forces on all atoms were below 0.05 eV/Å. The electronic structure was calculated using the Perdew–Burke–Ernzerhof (PBE) exchange-correlation functional using a Γ-centered k-point grid with a density of 12 Å and a plane wave energy cutoff of 800 eV. Spin–orbit coupling was included nonself-consistently[3] in the calculated band structure shown in Figure 2d but does not have a significant influence on the electronic structure of $CrBr_3$. The effective Hubbard correction used in this paper, $U_{eff} = U - J$, was applied to the d orbitals of chromium.

ASSOCIATED CONTENT

Supporting Information

The Supporting Information is available free of charge at https://pubs.acs.org/doi/10.1021/acsnano.3c01038.

Details for the sample preparation and characterization methods; DFT calculations details; band edge determination; carrier density determination (PDF)

AUTHOR INFORMATION

Corresponding Authors

Jiong Lu – *Department of Chemistry, National University of Singapore, Singapore 117543, Singapore; Institute for Functional Intelligent Materials, National University of Singapore, Singapore 117544, Singapore;* orcid.org/0000-0002-3690-8235; Email: chmluj@nus.edu.sg

Thomas Olsen – *Department of Physics, Computational Atomic-Scale Materials Design (CAMD), Technical University of Denmark, DK-2800 Kgs. Lyngby, Denmark;* Email: tolsen@fysik.dtu.dk

Authors

Pin Lyu – *Department of Chemistry, National University of Singapore, Singapore 117543, Singapore; Institute for Functional Intelligent Materials, National University of Singapore, Singapore 117544, Singapore;* orcid.org/0000-0003-1881-3766

Joachim Sødequist – *Department of Physics, Computational Atomic-Scale Materials Design (CAMD), Technical University of Denmark, DK-2800 Kgs. Lyngby, Denmark*

Xiaoyu Sheng – *Department of Chemistry, National University of Singapore, Singapore 117543, Singapore*

Zhizhan Qiu – *Department of Chemistry, National University of Singapore, Singapore 117543, Singapore; Institute for Functional Intelligent Materials, National University of Singapore, Singapore 117544, Singapore*

Anton Tadich – *ARC Centre for Future Low Energy Electronics Technologies, Monash University, Clayton, Victoria 3800, Australia; Australian Synchrotron, Clayton, Victoria 3168, Australia;* orcid.org/0000-0001-9455-5901

Qile Li – *ARC Centre for Future Low Energy Electronics Technologies and School of Physics and Astronomy, Monash University, Clayton, Victoria 3800, Australia;* orcid.org/0000-0001-7374-1692

Mark T. Edmonds – *ARC Centre for Future Low Energy Electronics Technologies and School of Physics and Astronomy, Monash University, Clayton, Victoria 3800, Australia;* orcid.org/0000-0001-8054-5470

Meng Zhao – *Institute of Materials Research and Engineering (IMRE), Agency for Science, Technology and Research (A*STAR), Singapore 138634, Republic of Singapore;* orcid.org/0000-0002-0584-9420

Jesús Redondo − *Institute of Physics of the Czech Academy of Sciences, 162 00 Prague 6, Czech Republic; Faculty of Mathematics and Physics, Charles University, 180 00 Prague, Czech Republic;* orcid.org/0000-0002-8147-689X

Martin Švec − *Faculty of Mathematics and Physics, Charles University, 180 00 Prague, Czech Republic;* orcid.org/0000-0003-0369-8144

Peng Song − *School of Electrical and Electronic Engineering and School of Materials Science and Engineering, Nanyang Technological University, Singapore 639798, Singapore*

Complete contact information is available at: https://pubs.acs.org/10.1021/acsnano.3c01038

Author Contributions

J.L. supervised projects. P.L. fabricated the device, grew the sample and performed STM measurements and data analysis with the help of X.S.; J.S. performed the density functional theory calculation under the supervision of T.O.; J.L. and P.L. prepared the manuscript with the contribution from J.S. and T.O. All authors contributed to the discussion and helped in writing the manuscript. P.L., J.S., and X.S. contributed equally.

Notes

The authors declare no competing financial interest.

ACKNOWLEDGMENTS

We acknowledge the valuable discussion with Shawulienu Kezilebieke and Peter Liljeroth on the growth of $CrBr_3$. This work was supported by MOE grants (MOE2019-T2-2-044, MOE T2EP50121-0008, MOE-T2EP10221-0005), Agency for Science, Technology and Research (A*STAR) under its AME IRG grant (Project715 no. M21K2c0113) and Villum foundation (grant no. 00029378).

REFERENCES

(1) Mühlbauer, S.; Binz, B.; Jonietz, F.; Pfleiderer, C.; Rosch, A.; Neubauer, A.; Georgii, R.; Böni, P. Skyrmion lattice in a chiral magnet. *Science* **2009**, *323* (5916), 915−919.

(2) Banerjee, A.; Bridges, C.; Yan, J.-Q.; Aczel, A.; Li, L.; Stone, M.; Granroth, G.; Lumsden, M.; Yiu, Y.; Knolle, J.; et al. Proximate Kitaev quantum spin liquid behaviour in a honeycomb magnet. *Nature materials* **2016**, *15* (7), 733−740.

(3) Deng, Y.; Yu, Y.; Shi, M. Z.; Guo, Z.; Xu, Z.; Wang, J.; Chen, X. H.; Zhang, Y. Quantum anomalous Hall effect in intrinsic magnetic topological insulator $MnBi_2Te_4$. *Science* **2020**, *367* (6480), 895−900.

(4) Huang, B.; Clark, G.; Navarro-Moratalla, E.; Klein, D. R.; Cheng, R.; Seyler, K. L.; Zhong, D.; Schmidgall, E.; McGuire, M. A.; Cobden, D. H.; et al. Layer-dependent ferromagnetism in a van der Waals crystal down to the monolayer limit. *Nature* **2017**, *546* (7657), 270−273.

(5) Gong, C.; Li, L.; Li, Z.; Ji, H.; Stern, A.; Xia, Y.; Cao, T.; Bao, W.; Wang, C.; Wang, Y.; et al. Discovery of intrinsic ferromagnetism in two-dimensional van der Waals crystals. *Nature* **2017**, *546* (7657), 265−269.

(6) Lado, J. L.; Fernández-Rossier, J. On the origin of magnetic anisotropy in two dimensional CrI_3. *2D Materials* **2017**, *4* (3), 035002.

(7) Tseng, C.-C.; Song, T.; Jiang, Q.; Lin, Z.; Wang, C.; Suh, J.; Watanabe, K.; Taniguchi, T.; McGuire, M. A.; Xiao, D. Gate-tunable proximity effects in graphene on layered magnetic insulators. *Nano Lett.* **2022**, *22*, 8495.

(8) Ghazaryan, D.; Greenaway, M. T.; Wang, Z.; Guarochico-Moreira, V. H.; Vera-Marun, I. J.; Yin, J.; Liao, Y.; Morozov, S. V.; Kristanovski, O.; Lichtenstein, A. I.; et al. Magnon-assisted tunnelling in van der Waals heterostructures based on $CrBr_3$. *Nature Electronics* **2018**, *1* (6), 344−349.

(9) Katoch, J.; Ulstrup, S.; Koch, R. J.; Moser, S.; McCreary, K. M.; Singh, S.; Xu, J.; Jonker, B. T.; Kawakami, R. K.; Bostwick, A.; et al. Giant spin-splitting and gap renormalization driven by trions in single-layer WS_2/h-BN heterostructures. *Nat. Phys.* **2018**, *14* (4), 355−359.

(10) Chia, X.; Pumera, M. Characteristics and performance of two-dimensional materials for electrocatalysis. *Nature Catalysis* **2018**, *1* (12), 909−921.

(11) Jiang, S.; Shan, J.; Mak, K. F. Electric-field switching of two-dimensional van der Waals magnets. *Nature materials* **2018**, *17* (5), 406−410.

(12) Jiang, S.; Li, L.; Wang, Z.; Mak, K. F.; Shan, J. Controlling magnetism in 2D CrI_3 by electrostatic doping. *Nature Nanotechnol.* **2018**, *13* (7), 549−553.

(13) Huang, B.; Clark, G.; Klein, D. R.; MacNeill, D.; Navarro-Moratalla, E.; Seyler, K. L.; Wilson, N.; McGuire, M. A.; Cobden, D. H.; Xiao, D.; et al. Electrical control of 2D magnetism in bilayer CrI_3. *Nature Nanotechnol.* **2018**, *13* (7), 544−548.

(14) Zhang, Z.; Shang, J.; Jiang, C.; Rasmita, A.; Gao, W.; Yu, T. Direct photoluminescence probing of ferromagnetism in monolayer two-dimensional $CrBr_3$. *Nano Lett.* **2019**, *19* (5), 3138−3142.

(15) Pollini, I. Electronic structure of $CrBr_3$ studied by X-ray photoelectron spectroscopy. *Phys. Rev. B* **1999**, *60* (23), 16170.

(16) Pollini, I. Coulomb correlation energy versus covalence in transition-metal compounds. *Journal of electron spectroscopy and related phenomena* **2006**, *152* (3), 107−114.

(17) Fumega, A. O.; Blanco-Canosa, S.; Babu-Vasili, H.; Gargiani, P.; Li, H.; Zhou, J.-S.; Rivadulla, F.; Pardo, V. Electronic structure and magnetic exchange interactions of Cr-based van der Waals ferromagnets. A comparative study between $CrBr_3$ and $Cr_2Ge_2Te_6$. *J. Mater. Chem. C* **2020**, *8* (39), 13582−13589.

(18) Gibertini, M.; Koperski, M.; Morpurgo, A. F.; Novoselov, K. S. Magnetic 2D materials and heterostructures. *Nature Nanotechnol.* **2019**, *14* (5), 408−419.

(19) Qiu, Z.; Holwill, M.; Olsen, T.; Lyu, P.; Li, J.; Fang, H.; Yang, H.; Kashchenko, M.; Novoselov, K. S.; Lu, J. Visualizing atomic structure and magnetism of 2D magnetic insulators via tunneling through graphene. *Nat. Commun.* **2021**, *12*, 70.

(20) Chen, W.; Sun, Z.; Wang, Z.; Gu, L.; Xu, X.; Wu, S.; Gao, C. Direct observation of van der Waals stacking-dependent interlayer magnetism. *Science* **2019**, *366* (6468), 983−987.

(21) Kezilebieke, S.; Huda, M. N.; Vaňo, V.; Aapro, M.; Ganguli, S. C.; Silveira, O. J.; Głodzik, S.; Foster, A. S.; Ojanen, T.; Liljeroth, P. Topological superconductivity in a van der Waals heterostructure. *Nature* **2020**, *588* (7838), 424−428.

(22) Kezilebieke, S.; Silveira, O. J.; Huda, M. N.; Vaňo, V.; Aapro, M.; Ganguli, S. C.; Lahtinen, J.; Mansell, R.; van Dijken, S.; Foster, A. S.; et al. Electronic and magnetic characterization of epitaxial $CrBr_3$ monolayers on a superconducting substrate. *Adv. Mater.* **2021**, *33*, 2006850.

(23) Soriano, D.; Katsnelson, M. I.; Fernández-Rossier, J. Magnetic two-dimensional chromium trihalides: a theoretical perspective. *Nano Lett.* **2020**, *20* (9), 6225−6234.

(24) Molina-Sánchez, A.; Catarina, G.; Sangalli, D.; Fernández-Rossier, J. Magneto-optical response of chromium trihalide monolayers: chemical trends. *Journal of Materials Chemistry C* **2020**, *8* (26), 8856−8863.

(25) Kashin, I.; Mazurenko, V.; Katsnelson, M.; Rudenko, A. Orbitally-resolved ferromagnetism of monolayer CrI_3. *2D Materials* **2020**, *7* (2), 025036.

(26) Chernikov, A.; Van Der Zande, A. M.; Hill, H. M.; Rigosi, A. F.; Velauthapillai, A.; Hone, J.; Heinz, T. F. Electrical tuning of exciton binding energies in monolayer WS_2. *Physical review letters* **2015**, *115* (12), 126802.

(27) Rigosi, A. F.; Hill, H. M.; Rim, K. T.; Flynn, G. W.; Heinz, T. F. Electronic band gaps and exciton binding energies in monolayer $Mo_xW_{1-x}S_2$ transition metal dichalcogenide alloys probed by scanning tunneling and optical spectroscopy. *Phys. Rev. B* **2016**, *94* (7), 075440.

(28) Gao, S.; Yang, L. Renormalization of the quasiparticle band gap in doped two-dimensional materials from many-body calculations. *Phys. Rev. B* **2017**, *96* (15), 155410.
(29) Liang, Y.; Yang, L. Carrier plasmon induced nonlinear band gap renormalization in two-dimensional semiconductors. *Physical review letters* **2015**, *114* (6), 063001.
(30) Zhang, Z.; Chen, Z.; Bouaziz, M.; Giorgetti, C.; Yi, H.; Avila, J.; Tian, B.; Shukla, A.; Perfetti, L.; Fan, D.; et al. Direct observation of band gap renormalization in layered indium selenide. *ACS Nano* **2019**, *13* (11), 13486−13491.
(31) Riis-Jensen, A. C.; Lu, J.; Thygesen, K. S. Electrically controlled dielectric band gap engineering in a two-dimensional semiconductor. *Phys. Rev. B* **2020**, *101* (12), 121110.
(32) Waldecker, L.; Raja, A.; Rösner, M.; Steinke, C.; Bostwick, A.; Koch, R. J.; Jozwiak, C.; Taniguchi, T.; Watanabe, K.; Rotenberg, E.; et al. Rigid band shifts in two-dimensional semiconductors through external dielectric screening. *Phys. Rev. Lett.* **2019**, *123* (20), 206403.
(33) Ugeda, M. M.; Bradley, A. J.; Shi, S.-F.; Da Jornada, F. H.; Zhang, Y.; Qiu, D. Y.; Ruan, W.; Mo, S.-K.; Hussain, Z.; Shen, Z.-X.; et al. Giant bandgap renormalization and excitonic effects in a monolayer transition metal dichalcogenide semiconductor. *Nature Mater.* **2014**, *13* (12), 1091−1095.
(34) Zhang, Y.; Brar, V. W.; Wang, F.; Girit, C.; Yayon, Y.; Panlasigui, M.; Zettl, A.; Crommie, M. F. Giant phonon-induced conductance in scanning tunnelling spectroscopy of gate-tunable graphene. *Nat. Phys.* **2008**, *4* (8), 627−630.
(35) Tenasini, G.; Soler-Delgado, D.; Wang, Z.; Yao, F.; Dumcenco, D.; Giannini, E.; Watanabe, K.; Taniguchi, T.; Moulsdale, C.; Garcia-Ruiz, A.; et al. Band Gap Opening in Bilayer Graphene-$CrCl_3$/$CrBr_3$/CrI_3 van der Waals Interfaces. *Nano Lett.* **2022**, *22* (16), 6760−6766.
(36) Zhou, B.; Balgley, J.; Lampen-Kelley, P.; Yan, J.-Q.; Mandrus, D. G.; Henriksen, E. A. Evidence for charge transfer and proximate magnetism in graphene-α- RuC_3 heterostructures. *Phys. Rev. B* **2019**, *100* (16), 165426.
(37) Rizzo, D. J.; Jessen, B. S.; Sun, Z.; Ruta, F. L.; Zhang, J.; Yan, J.-Q.; Xian, L.; McLeod, A. S.; Berkowitz, M. E.; Watanabe, K.; et al. Charge-transfer plasmon polaritons at graphene/α-$RuCl_3$ interfaces. *Nano Lett.* **2020**, *20* (12), 8438−8445.
(38) Zhang, J.; Zhao, B.; Zhou, T.; Xue, Y.; Ma, C.; Yang, Z. Strong magnetization and Chern insulators in compressed graphene/CrI 3 van der Waals heterostructures. *Phys. Rev. B* **2018**, *97* (8), 085401.
(39) Kvashnin, Y. O.; Rudenko, A. N.; Thunström, P.; Rösner, M.; Katsnelson, M. I. Dynamical correlations in single-layer CrI_3. *Phys. Rev. B* **2022**, *105* (20), 205124.
(40) Roy, S. B. *Mott Insulators*. IOP Publishing, 2019.
(41) Wu, J.; Yao, Y.; Lin, M. L.; Rösner, M.; Du, Z.; Watanabe, K.; Taniguchi, T.; Tan, P. H.; Haas, S.; Wang, H. Spin-phonon coupling in ferromagnetic monolayer chromium tribromide. *Adv. Mater.* **2022**, *34* (20), 2108506.
(42) Sarkar, S.; Kratzer, P. Magnetic exchange interactions in bilayer CrX_3 (X= Cl, Br, and I): A critical assessment of the DFT+ U approach. *Phys. Rev. B* **2021**, *103* (22), 224421.

https://doi.org/10.1021/acsnano.3c01038
ACS Nano 2023, 17, 15441−15448